

Supplementary Materials and Methods

Computational model of turtle scute development

The computational model is built by using an already known mechanism to build a pattern of regularly spaced gene expression spot domains. Reaction-diffusion systems are also an already known way to produce the expansion of those domains as traveling waves and their merging (Gierer and Meinhardt, 1972).

This model implements two coupled reaction-diffusion systems and growth in a two-dimensional epithelium representing the developing carapace. Each reaction-diffusion system includes two diffusible extracellular molecules. The activator A_1 for the first reaction-diffusion system promotes its own synthesis and that of its diffusible inhibitor I_1 . Equally, in the second reaction-diffusion system the activator A_2 promotes its own synthesis and that of its diffusible inhibitor I_2 . In addition, A_1 promotes the production of A_2 . The inhibitors repress the synthesis of their respective activators. The initial condition from which the simulations start includes two rows of A_1 concentration peaks (see Figs 1, 4) at the margins of the carapace. During the first 150000 iterations, the model includes only growth. At the end of that period starts the first reaction-diffusion system, and after 30000 iterations, an acceleration of growth, according to the development of *T. scripta*. 55000 iterations later, the second reaction-diffusion system is initiated.

Reaction-diffusion kinetics:

The reaction-diffusion equations are derived from the classic Meinhardt-Gierer equations (Gierer and Meinhardt, 1972).

$$(1) \quad \frac{\partial A_1}{\partial t} = \frac{r_1 A_1^2}{1 + k_I I_1} - m_1 A_1 + a_r + D_I \nabla^2 A_1$$

$$(2) \quad \frac{\partial I_1}{\partial t} = r_2 A_1^2 - m_2 I_1 + D_2 \nabla^2 I_1$$

$$(3) \quad \frac{\partial A_2}{\partial t} = \frac{s A_1^2 + r_3 A_2^2}{1 + k_2 I_2} - m_3 A_2 + D_3 \nabla^2 A_2$$

$$(4) \quad \frac{\partial I_2}{\partial t} = r_4 A_2^2 - m_4 I_2 + i_r + D_4 \nabla^2 I_2$$

Here, r_1 and r_2 describe the rate of activation by the activator A_1 , and r_3 and r_4 activation by A_2 . k_1 and k_2 describe the strength of inhibition of A_1 and A_2 production by I_1 and I_2 . a_r is a residual activation of A_1 , whereas s is the rate of activation of A_2 by A_1 . i_r is a residual activation of I_2 . m_1 , m_2 , m_3 , and m_4 give decay rates of the gene products A_1 , I_1 , A_2 , and I_2 . D_1 , D_2 , D_3 , and D_4 are the diffusion rates of A_1 , I_1 , A_2 , and I_2 .

These parameters are such that the first reaction-diffusion system establishes a pattern of spots of expression of A_1 and I_1 and the second produces traveling waves from these spots that collide with each other to form the hexagon-like scute morphologies. The simulations are performed on a growing grid of square cells (at maximal size this grid reaches $1.5 \pm 0.2 \times 10^2$ cells). Every cell is adjacent to four neighbors. Boundary conditions are closed (zero flux). Numerical integration is performed by the Euler method with $\delta = 10^{-3}$.

Formation of boundaries between scutes by traveling waves:

The second reaction-diffusion system establishes the locations of future scute boundaries. In it concentration peaks of activator (A_2) and inhibitor (I_2) propagate centripetally from the spots of high A_1 expression (cf. Fig. 3), which have been previously positioned as a Turing pattern by the first reaction-diffusion system.

The propagation of these peaks occurs as a traveling wave phenomenon that emerges from the reaction-diffusion system. The same equations are used in the first and second reaction-diffusion systems but in the second reaction-diffusion system, the activator diffuses faster than its inhibitor, i.e. $D_3 > D_4$. Auto-activation of the activator leads to a fast increase in the concentration of activator, and, with a small but important delay, of the inhibitor, which starts repressing the increase of the activator. Since the activator diffuses faster than the inhibitor, the relative increase of activator is highest at the edges of its spatial extension, where activator molecules have just arrived by diffusion but inhibitor has had not time to arrive yet (Fig. S3). Thus, the highest concentration of activator is found in a temporally extending concentric ring around the spots of high expression of A_1 . Consequently, an inhibitor wave is seen following the wave of activator concentration (Fig. S3A-B).

The traveling waves expanding from the center of each forming scute end up colliding with each other in space and, as a result, form the stable (non-traveling) boundaries between scutes (Fig. 3). The traveling waves can only spread where there is no inhibitor (since inhibitor I_2 inhibits the increase in A_2 concentration; Fig. S3B) and since each traveling wave of A_2 is followed by a traveling wave of I_2 , the waves stop traveling where they meet (and hence do not cross each other; Fig. S3C). Thus, in the meeting point between traveling waves, a boundary with high A_2 concentration is formed.

This concentration of A_2 at the boundary is higher than in either of the traveling waves from which it is formed. This is because when two waves of A_2 approach each other, the cells between them start to receive, by diffusing from both waves, more A_2 than if there was only one traveling wave approaching. Since in equation (3), the A_2

auto-activation is non-linear (quadratic), this additional A_2 allows the A_2 to reach fast relatively high concentrations before the inhibitor waves arrive. This is why these boundaries may be sufficiently distinct and stable to define the seams between scutes in development.

Margins and initial conditions:

The margins are defined as two 13 cell-wide fringes spanning from the anterior to the posterior of the carapace. The initial conditions consist of two rows of A_1 concentration peaks (see Figs 1, 4) in these margins of the carapace. These peaks of A_1 have a constant concentration over the simulation time. The remaining cells in the margins do not produce A_1 .

Growth:

Growth is implemented by adding cells in the midline. These additions occur at different rates along the anterior-posterior axis in a pattern derived from empirical observations. As a consequence, added cells displace a whole row of cells to the left and to the right from the midline.

From iteration 180000, growth rates double to represent an acceleration observed in carapace growth.

Bead experiments:

Beads are simulated by defining a position x,y (see Fig. S4 for the exact values) from which an additional amount of (a) A_1 , A_2 , I_1 or I_2 or (b) another factor B , upstream of one of these, diffuses with a rate of D_{BB} . In case (a), the additional amount of activator or inhibitor diffusing in each time step from the bead is added to the concentrations of A_1 , A_2 , I_1 or I_2 , respectively, in the position $[x,y]$ of the bead; in

case (b), B is added to or subtracted from the differential equation defining the change of concentration in the molecule affected by B. Since B represents an additional sort of molecule, it is given a diffusion rate D_B and degradation rate m_B . The time t_B when diffusion from the bead is initialized was set according to the respective *in vitro* experiment we wanted to simulate.

Natural and abnormal variation:

Configurations of scute numbers seen in species such as *Caretta caretta* or *Lepidochelys olivacea* can be found in the variational space of the model by increasing or decreasing the length of the anterior/posterior axis of the developing carapace.

In order to generate the scute anomalies reported in Figs 5, S7, and S8, we introduced two alternative changes in the model. In one (Fig. S7), the right half of the carapace gradually moves towards the anterior direction. The time at which this movement starts is t_{shift} . From then, the hemisphere is moved by one row every v_{shift} iterations and i_{shift} times, t_{shift} , v_{shift} and i_{shift} being model parameters. In the other (Fig. S8), lateral growth on the right side is, from the beginning, faster by a factor of add_R/add_L than growth in the left side. This means that the position-dependent rate at which cells were added along the midline is multiplied with add_R/add_L , respectively.

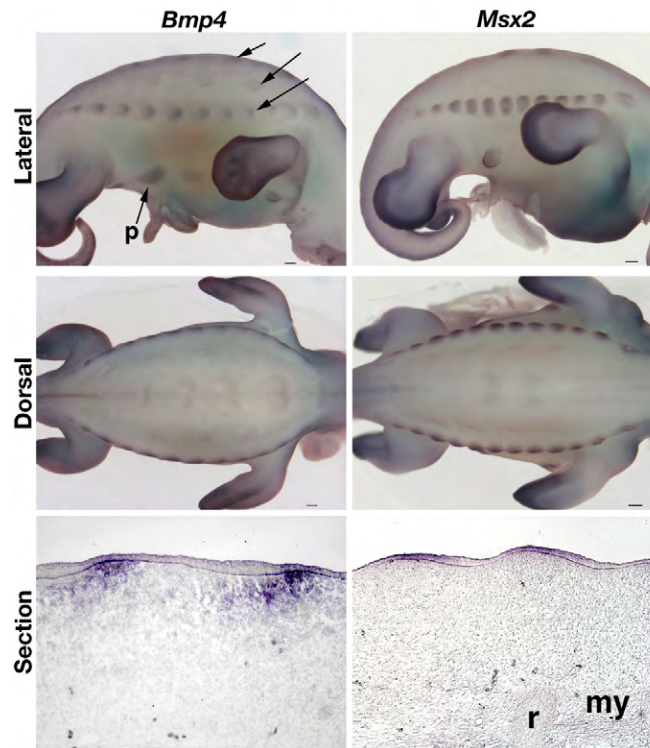


Fig. S1. Expression of *Bmp4* and *Msx2* viewed laterally, dorsally, and in section in stage Y16 *Trachemys* embryos. *Bmp4* and *Msx2* have overlapping expression patterns: the expression of *Bmp4* is stronger anteriorly in the developing scutes, whereas *Msx2* expression is seen along the protrusions of the carapacial ridge. Sections show that *Bmp4* is expressed in the mesenchyme and epithelium opposite the myotomes, and *Msx2* is expressed in the epithelium opposite the ribs. Arrows point to scute placodes. p, plastral scute placode; r, rib; my, myotome. Anterior is toward the right. Scale bars, 200 μ m.

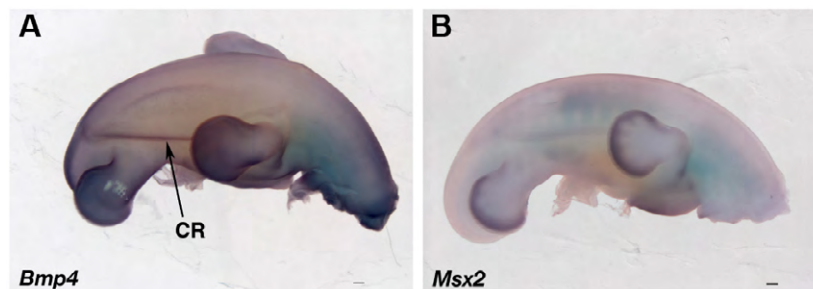


Fig. S2. Expression of *Bmp4* and *Msx2* in scuteless soft-shell *Pelodiscus* embryos. *Bmp4* and *Msx2* are expressed in a line along the carapacial ridge (CR). Anterior is toward the top. Scale bars, 200 μ m.

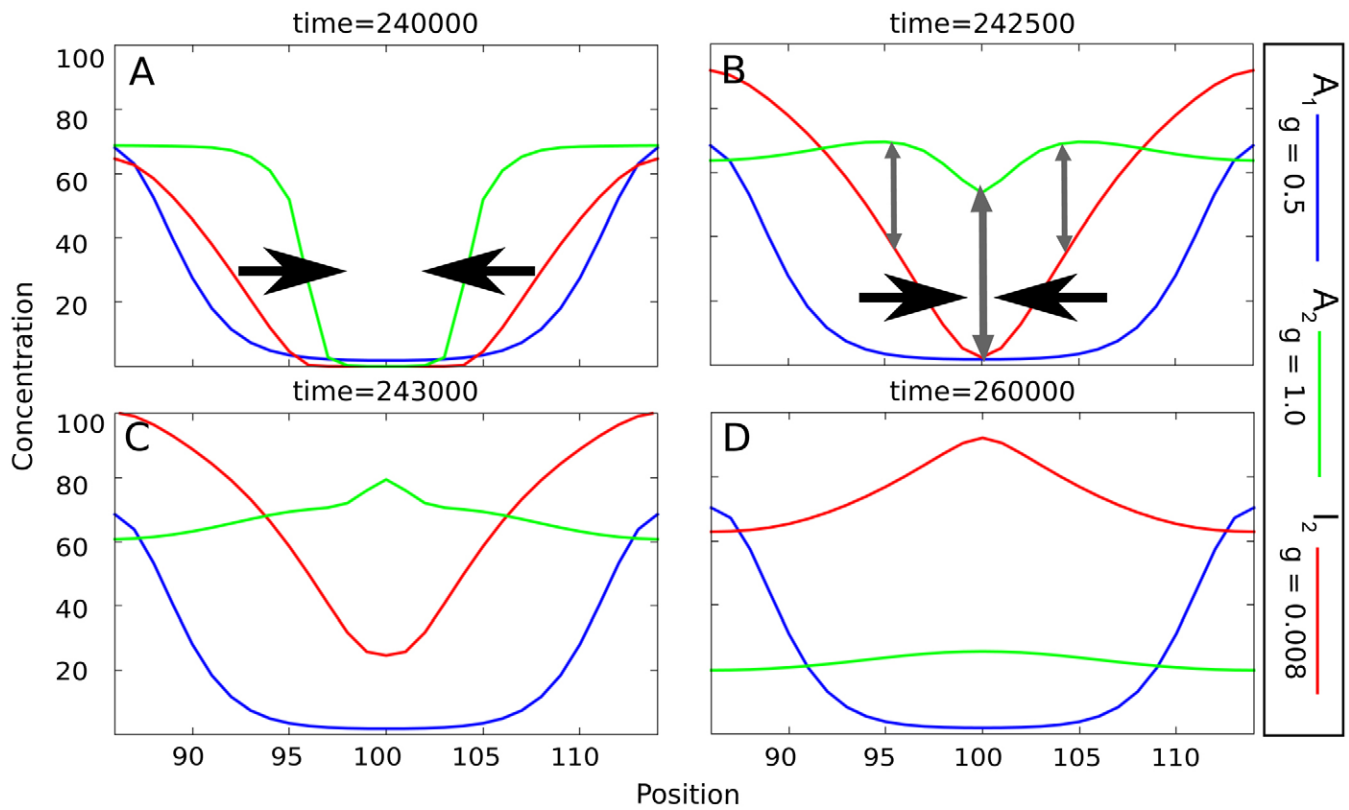


Fig. S3. 1-dimensional dynamics of colliding traveling waves. (A) From the spots of high A_1 , activator A_2 is produced and diffuses away. Due to its activation by A_2 , I_2 spreads with a delay. Vertical arrows stress the differences between A_2 and I_2 concentrations in different places; horizontal arrows indicate the direction of wave propagation. (B) While the waves approach due to diffusion, I_2 has already decreased A_2 concentration in those spots where it was produced first, preventing the A_2 wave from spreading backwards. This is why colliding waves stop (C). The contribution of both waves causes the difference between $[A_2]$ and $[I_2]$ to be highest at the collision point, leading to strong upregulation of A_2 . This leads to a relatively stable gene expression peak in this place (D). A_1 :blue lines; A_2 :green lines; I_2 :red lines. In all 1-dimensional graphs $Y=20$; $84 < X < 116$. For clearer visualization, we set $m_3=m_4=0.1$, $r_2=0.25$, and rescaled the concentration of A_1 in the graph by the factor $g=0.5$, I_2 by the factor $g=0.008$.

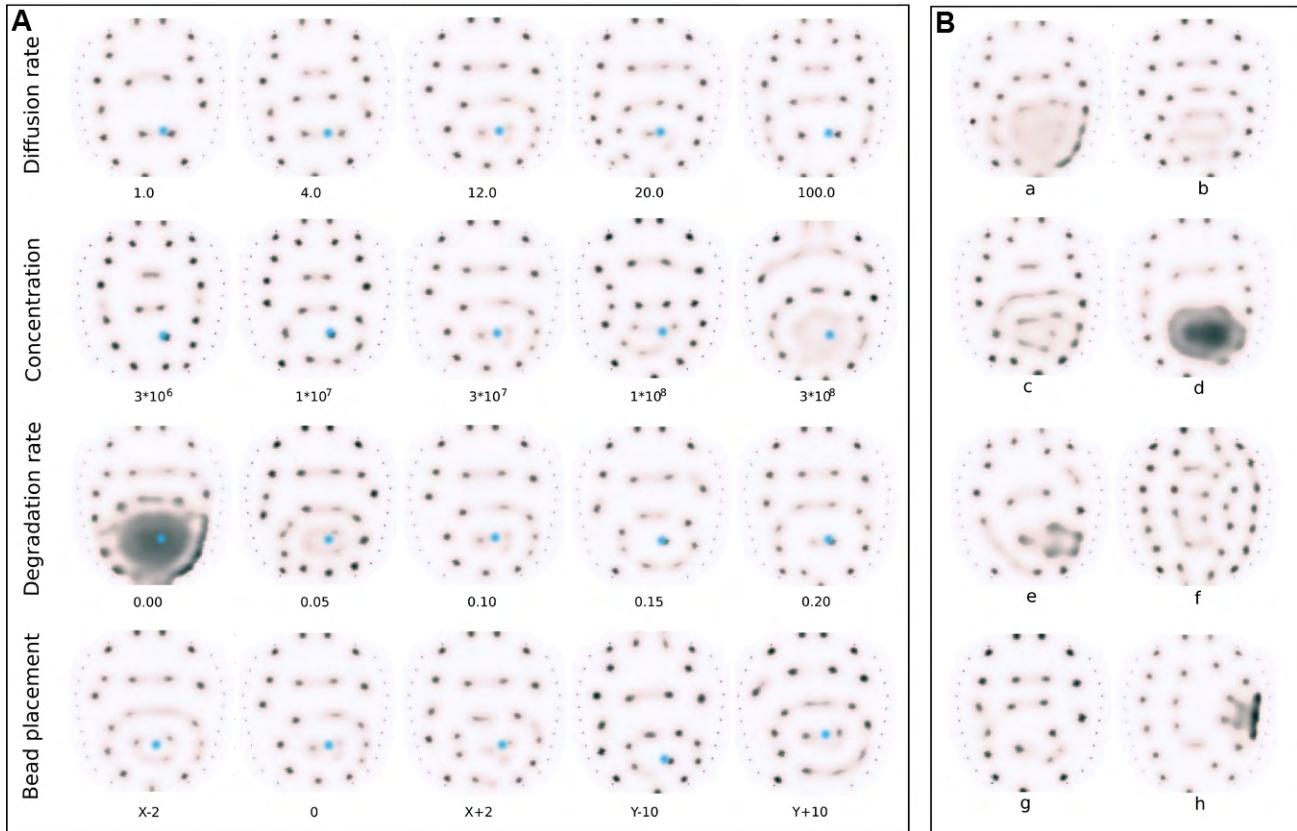


Fig. S4. Simulation of Inhibition of I_1 by bead implantations in a 5-dimensional parameter space. (A) For the basic model parameters given in the methods, a diffusible Factor B was allowed to diffuse from a certain position (X,Y) with a diffusion rate D and a degradation rate μ . The initial concentration in the bead is defined by B(0). For the comparison with a SHH-bead experiment shown in Figure 4, the following parameters were chosen: $D=12.0$, $\mu=0.1$, $B(0)=3 \times 10^7$, $X=40$, $Y=105$. Here, in every row, one parameter has been changed in the way indicated. The plots show the concentration of A, at $t=210000$. Units are AU. Bead positions are marked blue. (B) An overview of patterns produced by different combinations of the parameters listed above. a) $D=15.0$, $\mu=0.01$, $B(0)=2 \times 10^7$, $X=45$, $Y=111$. b) $D=15.0$, $\mu=0.05$, $B(0)=3 \times 10^7$, $X=40$, $Y=103$. c) $D=15.0$, $\mu=0.01$, $B(0)=1 \times 10^7$, $X=43$, $Y=109$. d) $D=5.0$, $\mu=0.01$, $B(0)=3 \times 10^7$, $X=40$, $Y=107$. e) $D=5.0$, $\mu=0.01$, $B(0)=1 \times 10^7$, $X=45$, $Y=113$. f) $D=100.0$, $\mu=0.0$, $B(0)=1 \times 10^7$, $X=65$, $Y=110$. g) $D=5.0$, $\mu=0.1$, $B(0)=3 \times 10^7$, $X=45$, $Y=105$. h) $D=4.0$, $\mu=0.0$, $B(0)=1 \times 10^7$, $X=65$, $Y=110$.

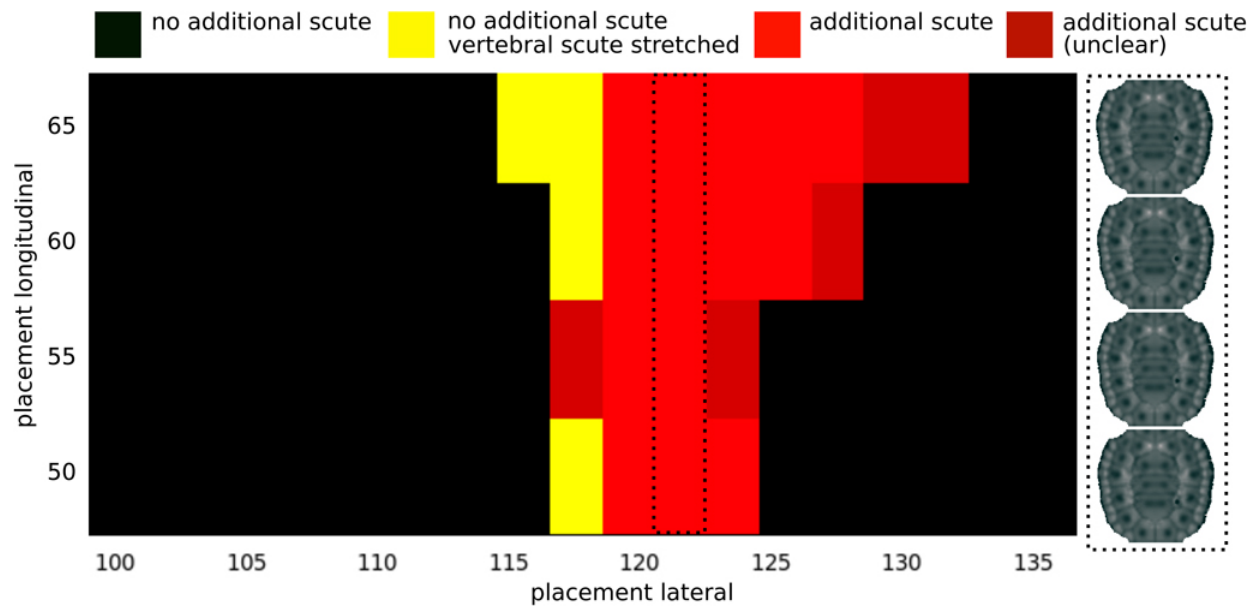


Fig. S5. Simulation of Activation of A_2 by bead implantations. For the basic model parameters, A_2 was allowed to diffuse from a bead position X, Y and an initial concentration $A_2(0)=10^5$. The figure shows the morphospace for different positions of the bead. It can be shown that the total variation obtained is relatively low, since only three distinct types of morphologies emerge: lengthening of vertebral scutes, one additional scute, and the normal phenotype. The parameter range in which additional scutes emerge is limited so that it highly depends on the placement of the bead whether or not any phenotypic change is obtained at all. The plots show the concentration of A_2 at $t=240000$; their position in the parameter space plot is delineated by spotted lines. A lateral position of $x=100$ localizes the midline.

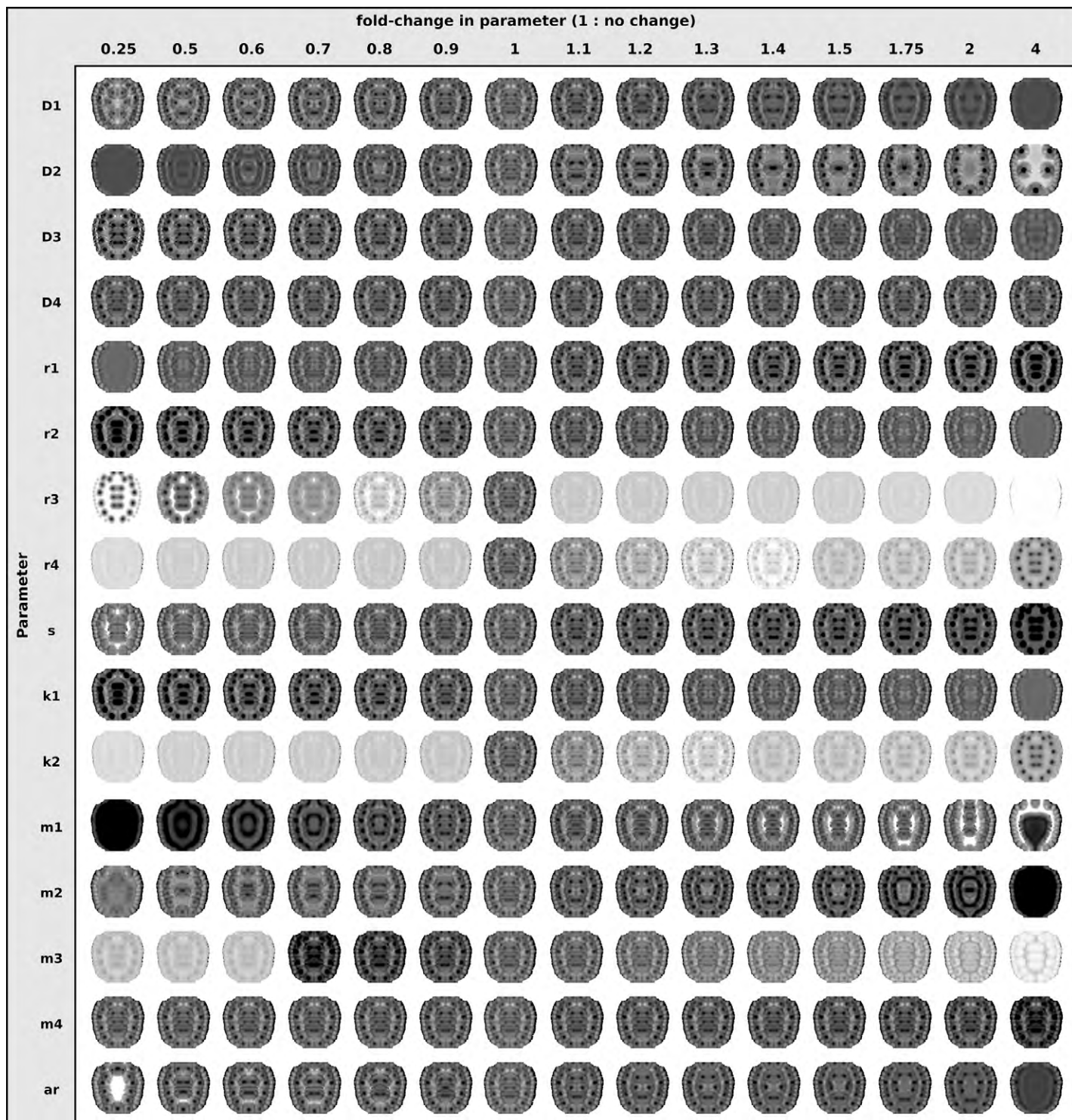


Fig. S6. Variation by parameter choices. All relevant parameters, as explained in supplementary materials and methods text, were individually modified by multiplying the original values by factors between 0.25 – 4.0, as noted on the horizontal axis. The plots show concentration of A_2 at time=240000, if run with the respective parameter value.

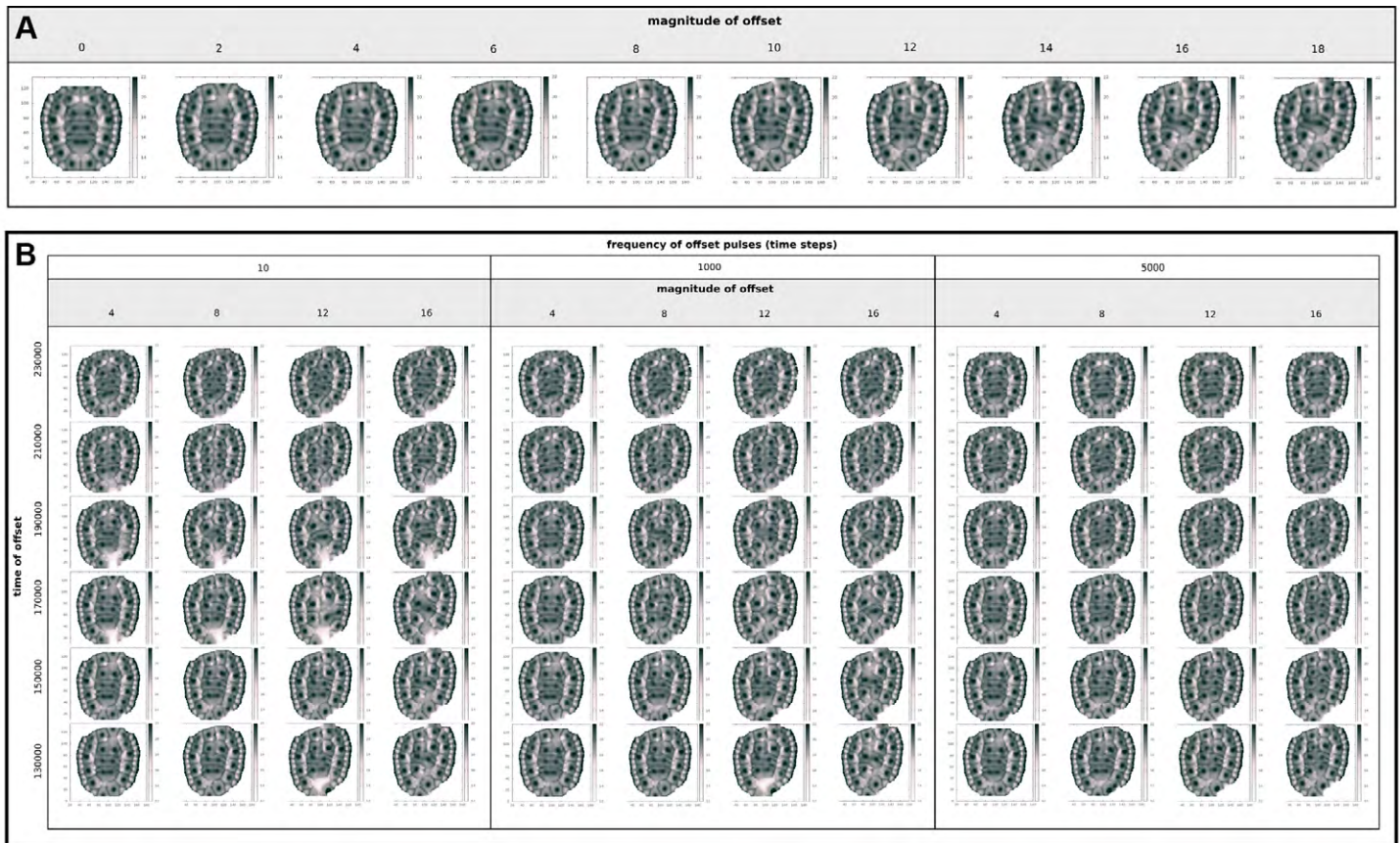


Fig. S7. Variational space of resulting scute patterns from the introduction of lateral offsets to the prepattern in the model. (A) A slight offset of various magnitudes (total number of cell rows shifted) to the right side in the anterior direction was immediately introduced into the pre-pattern. (B) Both the time (y-axis) and the frequency of offset pulses (every 10, 1000 and 5000 time steps; 3 panels) were varied in addition to the magnitude of offset (4 columns per panel). Time is given in simulation steps. The magnitude of offset is quantified in terms of grid cells shifted. In all pictures, the final expression of A2 is shown.



Fig. S8. Variational space of resulting scute patterns from the introduction of differential growth in the model. The introduction of differential growth to the model such that one side grows at different rates than the opposite side produces supernumerary scutes asymmetrically in varying patterns. The rates of growth acceleration in the left or right hemisphere are given by the figure axes.

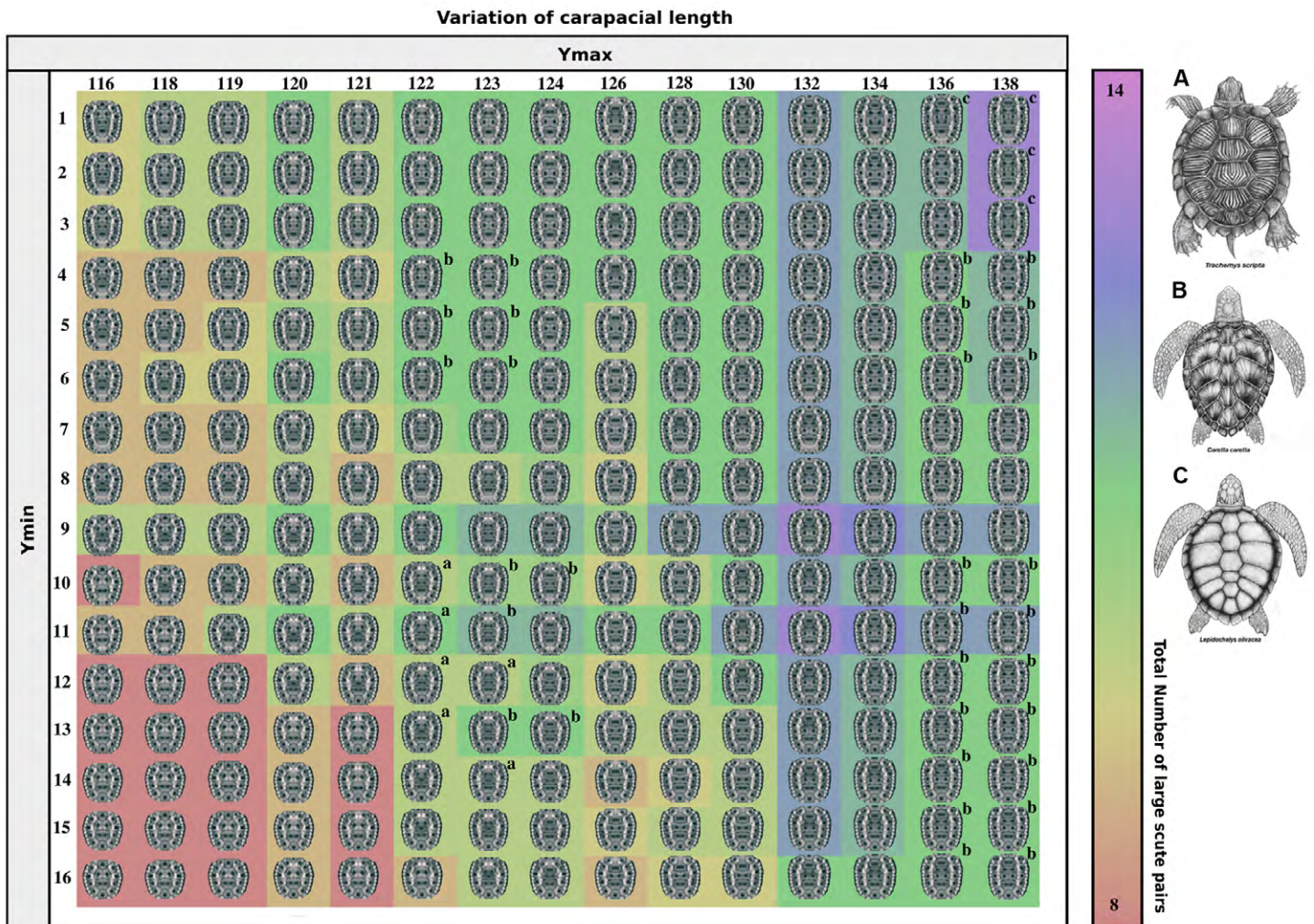
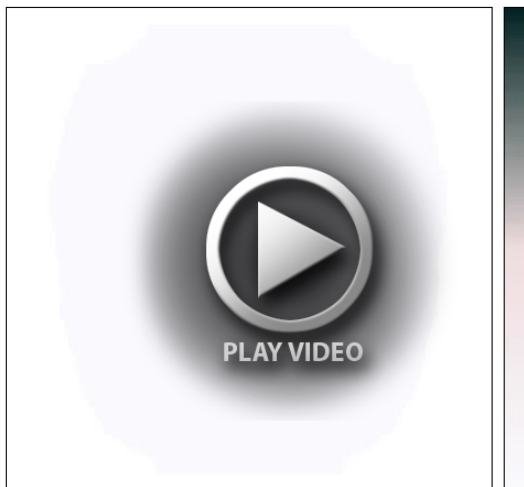


Fig. S9. Natural interspecific variation in scute numbers reproduced by the model. Most turtles have 4 costal and 5 vertebral scutes, as seen in *Trachemys scripta* (A). Some sea turtles, such as *Caretta caretta* (B) and *Lepidochelys olivacea* (C) have 5 or 6-7 costal scutes, respectively. *L. olivacea* also has an additional vertebral scute. By shortening or lengthening the anterior/posterior axis prior to the induction of the marginal scute placodes, additional costal and vertebral scutes are produced. Here, the axes of the figure assign the position of the anterior (Ymax) and posterior (Ymin) boundaries of the carapace. Colors illustrate the total number of vertebral scutes and costal scute pairs. Scute configurations that correspond to the numbers observed in these species have been marked with corresponding letters a, b, c and outlined. Independently of the subjectivity of the process of counting, the scute number is not correlated with an elongation of the anterior/posterior axis in a simply linear manner. Therefore, there are several possible trajectories to evolve from the configuration of *T. scripta* to the configuration of *C. caretta* within the morphospace.



Movie 1. Micro-computed tomography. Stage Y16 *Trachemys* fixed in 4% PFA and dyed with phosphotungstic acid in 70% ethanol for 24 hours (Metscher, 2009). The sample was imaged with a custom-built μ CT system Nanotom 180 NF to obtain scans with an effective voxel size of 5 μ m. The reconstruction was then down-sampled to 10 μ m voxel resolution and Avizo Fire 6.3 was used to render the 3D movies. iMovie 11 (Apple) was used to join the frontal (left) and lateral (right) movies. In the lateral movie, anterior is right.



Movie 2A.



Movie 2B.

Movie 2. Movie of the mathematical models of turtle scute formation. (A) From a pre-pattern of 12 marginal spots at $t=0$, a first activator-inhibitor coupled with growth (shown left) sets the relative positions of the presumptive scute placodes, resulting in two columns of 12 marginal, 4 costal, and 6 vertebral scute primordia ($t=230000$). A second reaction-diffusion system (shown right), activated by the first reaction-diffusion system, generates the final scute architecture by traveling waves, resulting in 24 marginal, 8 costal, and 6 vertebral (5 vertebral plus 1 nuchal) scutes, as seen in *Trachemys*. (B) High time resolution version of the second reaction-diffusion system to better illustrate its properties. FFmpeg (<http://ffmpeg.org/>) was used to create these movies.